

Available online at www.sciencedirect.com



journal homepage: www.elsevier.com/locate/jmrt



Original Article

Scale and size effects on the mechanical properties of bioinspired 3D printed two-phase composites



Frances Y. Su^b, Fereshteh A. Sabet ^a, Katherine Tang^b, Sean Garner^b, Siyuan Pang^a, Michael T. Tolley^b, Iwona Jasiuk^{a,*}, Joanna McKittrick^{b,1}

ARTICLE INFO

Article history: Received 22 June 2020 Accepted 15 October 2020 Available online 24 October 2020

Keywords:
Scale effects
Size effects
3D-printing
Interpenetrating phases
Two-phase composites
Architectured materials

ABSTRACT

Multi-material 3D printing offers design flexibility for the manufacture of new architectured composite materials and has been increasingly used to explore the mechanical properties of bioinspired composites. In this study, the influence of scale and size on mechanical properties of periodic two-phase composites with various architectures of a stiff and a soft phase are explored. The studied composites include an interpenetrating phase composite with two continuous phases (inspired by bone), a matrix-inclusion composite with a continuous and a discontinuous phase, and a discontinuous phase composite where both phases are discontinuous. These composites are fabricated by additive manufacturing, and their mechanical properties are evaluated experimentally using a compression test complemented by digital image correlation, and numerically through finite element analysis. Overall trends show that the elastic moduli and yield strengths decrease as the scale is increased. Our results on size effects reveal an increase in elastic modulus and yield strength with increasing size of the sample. Our investigation outcomes help to better understand some of the challenges in studying and applications of additively manufactured composites and shed light on scale and size effects on mechanical properties of 3D printed two-phase composites. This paper illustrates a need for further studies of scale and size effects in additively manufactured materials. © 2020 The Authors. Published by Elsevier B.V. This is an open access article under the CC BY-NC-ND license (http://creativecommons.org/licenses/by-nc-nd/4.0/).

1. Introduction and background

Within the last decade, additive manufacturing (AM) has become a powerful tool for studying cellular and composite

materials with complex architectures and microstructures [1,2]. In particular, 3D printing has been used for fabricating bioinspired materials and structures. For example, the reason for the square cross-section of the seahorse tail was explored by comparing 3D printed tails with square and round cross-

^a Department of Mechanical Science and Engineering, University of Illinois at Urbana Champaign, 1206 West Green Street, Urbana, IL, 61801, USA

^b Department of Mechanical and Aerospace Engineering and Materials Science and Engineering Program University of California, San Diego 9500 Gilman Dr., La Jolla, CA, 92093-0411, USA

^{*} Corresponding author.

E-mail address: ijasiuk@illinois.edu (I. Jasiuk).

¹ Professor Joanna McKittrick was a wonderful mentor, collaborator, and friend. She was dedicated to advancing and training women scientists and she was particularly proud of our collaborative group, which is composed predominantly of women scientists. Her contributions to this paper cannot be overstated and she is missed dearly.

sections [3]. Square tails were shown to increase the resilience of the tail and impact resistance to crushing forces compared to round tails. 3D printing was also employed to adapt the mouthpiece of the sea urchin for use as a sediment sampler [4]. Nacre and bone, among other natural materials, have also been important sources of bioinspiration for designs of new, 3D printed composites. Previous work has investigated their fracture toughness [5,6], impact resistance [7], and energy dissipation [8] through 3D printed analogues. A bioinspired design incorporating two levels of the hierarchy of nacre showed that the impact resistance improved dramatically over only having one level of nacre structure [9]. Inspired by the stiffness gradients at the interface of the rigid ring teeth in squid suckers, functional stiffness gradients were found to minimize stress concentrations at the interfaces between 3D printed soft and rigid components [10]. Similarly, stiffness gradients were found to reduce the chance of interfacial failure upon the impact of jumping, 3D printed soft robot [11]. Mechanical properties of materials of other organisms have also been studied, such as the effect of ammonite suture geometries on interface properties [12,13], the fracture resistance of whale baleen [14], and mechanics of helicoidal fiber structures of the mantis shrimp dactyl club [15]. A recent review [16] provides a framework for using AM for bioinspiration.

AM has also been a vehicle for evaluating the effect of microstructures (architectures) on the mechanical properties of composite materials with stiff and soft phases. The effects of connectivity of phases on elastic modulus and stress and strain distributions have been investigated [1,17]. Composites with two interpenetrating (connected) phases were found to have superior mechanical properties to composites with inclusions [17]. Nacre, which is generally thought to primarily have a brick and mortar structure of ceramic plates and protein, actually contains mineral bridges between adjacent ceramic plates. Studies of nacreinspired 3D printed composites show that mineral bridges help maintain stiffness and improve the toughness of composites [18].

Multi-material 3D printing has been useful for studying the architectures of composites as it allows the flexibility of designs and ease of manufacture of materials with desired geometries. Also, printers can blend different polymers to achieve more fine-tuned material properties [17]. However, given that the technology is still in development, some shortcomings and artifacts are present in the resulting prints. For example, Yap et al. [19] found that dimensional accuracy was dependent on the printing orientation, position on the printing surface, and surface finish of the print (glossy or matte). Material properties of 3D printed materials are dependent on print conditions, AM technique used (e.g., extrusion-based, material jetting, powder bed fusion), dimensions of the sample, and other factors [20]. Bass et al. [21] showed that the print orientation has a more pronounced effect on material anisotropy of soft materials than stiff materials. The effect of aging on the tensile properties of 3D printed polymers was also explored, and tensile properties showed no change until the sixth week, after which the tensile strength and elastic modulus increased [21]. While the influence of printing parameters on mechanical properties has been explored, most studies focused on the properties of a single material. Moreover, there is a dearth of literature on size and scale effects in 3D printed composites. Understanding of the size and scale effects on mechanical properties of 3D printed materials is needed for interpretation of results and accurate determination of properties.

Boundary conditions generally influence experimental and computational results when the sample size is smaller than a representative volume element (RVE). In such a case, apparent properties are obtained (measured or computed) instead of effective properties [22]. The RVE is defined, following Hill [23], "as a region large enough so that the size of inclusions is much smaller than the size of the sample and overall material properties do not depend on boundary conditions." When a sample size used in experiments or a region used in computations of properties is smaller than the RVE, then the properties are bound from above by the results obtained using displacement boundary conditions and from below by those computed using traction boundary conditions [21,24-27]. Mixed boundary conditions, generally applied in experiments, give results that fall between these two bounds. Thus, the apparent properties depend on the size of the sample (region) and boundary conditions; these are called scale and boundary conditions effects. For periodic composites, the application of periodic boundary conditions in computations results in effective properties.

In this paper, we investigate the *scale effects* (by varying number of unit cells while keeping samples' volume/size constant) and size *effects* (using samples with a single unit cell and changing their volume/size) on mechanical properties of cubic, periodic two-phase composites with several different architectures. We conduct this study experimentally by 3D printing three types of composites of a stiff and soft phase:

- Discontinuous phase composite (DPC) with two discontinuous phase,
- Matrix-inclusion composite (MIC) with one continuous phase and one discontinuous phase (cubic inclusions), and
- 3) Interpenetrating phase composite (IPC) with two continuous phases.

Our prior study focused on the effect of the geometrical arrangement of phases on the mechanical behavior of such composites [28]. We found that a continuous stiff phase increases the elastic modulus and that compressive load is carried mainly by the stiff phase. In contrast, the soft phase contributes to the deformation of these composites. That study also investigated these composite models in the context of bone and found a good agreement between computational results using the IPC model and experimental measurements of bone at the microscale.

In the present study, we vary the size and number of unit cells to understand their effects on the mechanical properties of 3D printed composite materials and compare these results to those of finite element (FE) simulations. Such knowledge is needed for the fundamental understanding of the measured or computed properties of 3D printed composites so they can be safely used in technological and medical applications. Such insight can also benefit future experimental and computational studies of AM materials, and architectured materials in

general, and contribute to further advancements in the 3D printing industry.

2. Materials and methods

2.1. 3D printing and optical microscope imaging

Unit cell geometries of the composites were created in Solidworks (Dassault Systèmes, Vélizy-Villacoublay, France) and printed using an Objet 350 Connex3 printer (Stratasys, Poway, CA, USA) in Digital Materials Mode, which deposits layers of material with a thickness of ~30 μm. The materials used were VeroClear, which represents the stiff phase, and TangoBlack+ representing the soft phase. Three types of twophase periodic composites were printed: a DPC, a MIC, and an IPC, all with a 50% volume fraction of each phase (Fig. 1), following [28]. In DPC and MIC composites, the phases were also interchanged, leading to five cases. Samples made of only one phase (stiff or soft) were also printed to measure each phase's properties. All samples were printed with the "matte" setting to ensure a uniform support material coverage instead of a glossy setting, which uses the support material at the bottom but no support material on other surfaces when printing a cube sample. After printing, support material was removed from samples using a high-pressure water jet and scraping off support material. To ensure adequate support material removal for small samples, such as those with edge lengths 3.18 mm and 1.58 mm, an optical microscope was used to look at the samples. Specimens were allowed to dry at least 12 h before testing. Samples were tested over the course

of a few weeks due to their large number and were kept away from light during storage before testing to prevent exposure to ultraviolet (UV) light, which is used during printing to crosslink the printed polymers [29].

Surfaces of VeroClear and TangoBlack+ samples were imaged using a Keyence VK-X1000 3D Laser Scanning Confocal Microscope (Keyence, Itasca, IL, USA) with objective lenses ranging from 5X to 20X. A 3D surface profile was created using a 405-nm laser to measure the sample surface through widefield focus variation and was processed using the instrument's embedded software. One sample of each VeroClear size was imaged and one TangoBlack+ sample with edge length 6.35 mm was imaged. The thicknesses of aggregate layers were measured using ImageJ.

2.2. Mechanical testing and analysis

Quasi-static compression tests were performed according to ASTM Standard D695-15 [30] at a strain rate of 0.51% min⁻¹. Sample geometry was changed from 2:1 to 1:1 length:width ratio compared to the ASTM standard since some samples were prone to buckling and slippage. Samples were tested so that the printing direction, which dictates lamellar alignment, was perpendicular to the compressive load. This protocol was followed to avoid layer effects of the stiff VeroClear material when compressed parallel to the direction of printing due to the innate microstructural features from layer-by-layer printing. It is important to note that while the failure mode of VeroClear tends to differ between samples compressed perpendicular (buckling) and samples compressed parallel to the print direction (splitting), the anisotropy of the material

		1x1x1	2x2x2	4x4x4	8x8x8
Discontinuous phase composite	-				
Matrix-inclusion composite	Soft frame				
	Stiff frame				
Interpenetrating composite	Soft frame				
	Stiff frame				

Fig. 1 — Types of unit cells from left to right showing increasing number of unit cells. Each composite has a 0.5 volume fraction.

properties is minimal (<5%) [31,32]. The testing order of specimens was randomized using a random number generator. A linear fit was applied to determine the elastic modulus of samples. Average curves were plotted by interpolating stress-strain curves at evenly spaced intervals.

Two sets of compression experiments were conducted:

- (a) Same-sized samples $(12.7 \times 12.7 \times 12.7 \text{ mm}^3)$ with different numbers of unit cells including a single unit cell $(1 \times 1 \times 1)$, $2 \times 2 \times 2$, $4 \times 4 \times 4$, and $8 \times 8 \times 8$ shown in Fig. 1.
- (b) Individual unit cells with edge lengths of 12.7, 6.35, 3.18, and 1.58 mm that correspond to the edge lengths of single-unit cells in the samples in set (a).

The set (a) explored the effects of scale by increasing the number of unit cells while keeping the size of samples the same. The set (b) gave the mechanical properties of samples of different sizes but having only a single unit cell. The minimum feature size (i.e., outer later in MICs or side strut in IPCs) was ~0.21 mm, which is almost an order of magnitude larger than the resolution of the 3D printer ~0.030 mm. Six samples were printed for each sample type in the experimental set (a), and three samples were printed for each sample type in the set (b) after the set (a) showed low variation in mechanical properties. The smaller samples (6.35, 3.18, and 1.58 mm edge lengths) were tested with an MTS Insight electromechanical testing system with a 2000 N load cell (MTS system Corp., Eden Prairie, MN). The larger samples (25.4, 12.7, and 6.35 mm edge lengths) were tested with an Instron 3367 load frame (Instron, Norwood, MA, USA) with a 30 kN load cell so that experimental loads were appropriate for the load cells used. The 6.35 mm samples were tested using both load cells to ensure consistent results between the two load cells. The 6.35 mm samples tested with the 2000 N load cell are denoted as 6.35 mm-A, and the 6.35 mm samples tested with the 3000 N load cell are denoted as 6.35 mm-B. The yield stress was defined as the maximum stress before buckling, before a resulting drop in stress occurs. The yield strain is reported as the strain at the defined yield stress. For samples that did not have a clear yield point, yield stress and strain were not reported.

The digital image correlation (DIC) method was performed on the samples to obtain strain fields. Compression tests were recorded using a Coolpix L830 (Nikon Inc, Tokyo, Japan) at 720p and 30 fps. Videos were cropped and processed using a Matlab script so that every 25th frame was converted to a TIFF image. Ncorr [33] was used for DIC to look at planar (2D) displacement and strain maps. First, a reference image was loaded, and then a region of interest was selected as the sample surface facing the camera. DIC parameters such as subset radius and spacing were changed according to the sample but had values of approximately 25 and 5 pixels, respectively. Step analysis with seed propagation and auto propagation of seeds was enabled.

2.3. Finite element modeling

The composites were also modeled using FE software Abaqus (v. 6.14). Two sets of simulations were performed to

complement and verify the results obtained from the two sets of experiments. The stiff and soft polymers were modeled as elastic-plastic and non-linear hyperplastic materials, respectively. In the first set of simulations, the mechanical properties of constituent phases of set (a) samples were used: Young's modulus (E) of 1.22 GPa and yield strength of 67.3 MPa were used for the stiff phase after which a perfectly plastic behavior was assumed. In the second set of simulations, the properties obtained from set (b) samples were utilized: E and yield strength were 1.07 GPa and 67.0 MPa for the stiff polymer. These properties were obtained by testing samples with edge lengths of 12.7 mm, and are listed in Table 1; the values provided by the manufacturer are included for comparison. Poisson's ratio of 0.41 was used for the stiff polymer in both sets of simulations. The soft phase was modeled using Yeoh formulations [34]. The Yeoh model, also called the third-order reduced polynomial form, is used to describe isotropic incompressible rubber-like materials. In this model, the strain energy function (W) is described by Eq. (1):

$$W = \sum_{i=1}^{3} C_{i0} (I_1 - 3)^i$$
 (1)

where C_{i0} are material parameters I_1 and is the first strain invariant. The Yeoh model depends only on the first strain invariant, as given in Eq. (1). There are two options for inputting properties into the Yeoh model in Abaqus software. The first option is to enter coefficients of the model while the second option is to input stress-strain results directly, and the software calculates the coefficients for the model. In this study, the experimental test results on the soft polymer were directly entered into Abaqus. Poisson's ratio of 0.495 was used for the soft polymer as provided by the manufacturer.

Two interfaces boundary conditions were considered. First, the interfaces between stiff and soft phases were assumed to be perfectly bonded, and the models were analyzed under compression. Then, MICs and IPCs were simulated, allowing free slippage/separation at interfaces. Hard contacts were set up in the normal direction, while frictionless slip was assumed in the tangential direction. The DPC was not modeled, assuming free slippage interfaces, as the structure would not stay together without bonding at interfaces. It was observed that assuming the free slippage/separation at interfaces did not significantly affect the overall modulus or maximum obtainable stress for MIC and IPC. In the DPC model, each cubic block of material (either soft or stiff) was imported separately into Abaqus, and then proper constraints (perfect bonding) were applied at the interfaces. Another

Table 1 — Mechanical properties of the stiff polymer (VeroClear) given by the manufacturer and obtained from experiments (a) and (b). Sample size is 12.7 mm for both experiments (a) and (b). Values are given as average (standard deviation (s.d.)). Six samples of each polymer were tested.

	E (MPa)	Compressive yield strength (MPa)
Manufacturer [52]	2000-3000	_
Experiments (a)	1220 (40)	67.3 (0.7)
Experiments (b)	1068.9 (17.0)	67.0 (2.1)

Table 2 – Surface area of the interface between the two phases to volume ratio of the overall sample with dimensions 12.7 \times 12.7 \times 12.7 mm³. Units are in mm⁻¹.

	$1 \times 1 \times$	$2\times2\times$	$4\times4\times$	$8 \times 8 \times$
	1	2	4	8
Discontinuous Phase Composite	0.24	0.71	1.65	3.55
Matrix-inclusion Composite	0.29	0.59	1.18	2.36
Interpenetrating Phase Composite	0.24	0.47	0.94	1.89

option is to import all four blocks of each phase as a whole, in which case a stiffer response is expected. Ten-node quadratic tetrahedron elements (C3D10) were used to mesh the models, and a mesh convergence study was done for each geometry to ensure adequate fineness of the mesh.

The compression test was simulated by applying mixed boundary conditions (MBCs) to represent the experimentally applied boundary conditions. Sidewalls were traction free, the base platen had zero displacements, while the top platen had zero horizontal displacements and an applied vertical displacement. The conditions reflected the high surface roughness at both platens and assumed no slip. By increasing

the number of unit cells in experiments (a), the results should approach those obtained by periodic boundary conditions (PBCs) applied to a unit cell. Thus, PBCs were also used to compare the results with those from experiments (a).

3. Results and discussion

3.1. Scale effects: increasing number of unit cells for a constant sample size

The first set of samples tested (set (a)) included the five types of model composites with four different numbers of unit cells $(1 \times 1 \times 1, 2 \times 2 \times 2, 4 \times 4 \times 4, \text{ and } 8 \times 8 \times 8)$ in a given sample while keeping the overall test sample size constant $(12.7 \times 12.7 \times 12.7 \text{ mm}^3)$. These experiments allowed us to study scale effects, namely, the effect of the number of unit cells while keeping the overall samples size constant (which resulted in changing the size of a unit cell) on apparent mechanical properties. Following Huet [22], effective properties are approached by increasing the number of unit cells.

Stress-strain curves (Fig. 2) are separated by composite type and include results from same-sized samples with different numbers of unit cells and FE modeling for $1 \times 1 \times 1$

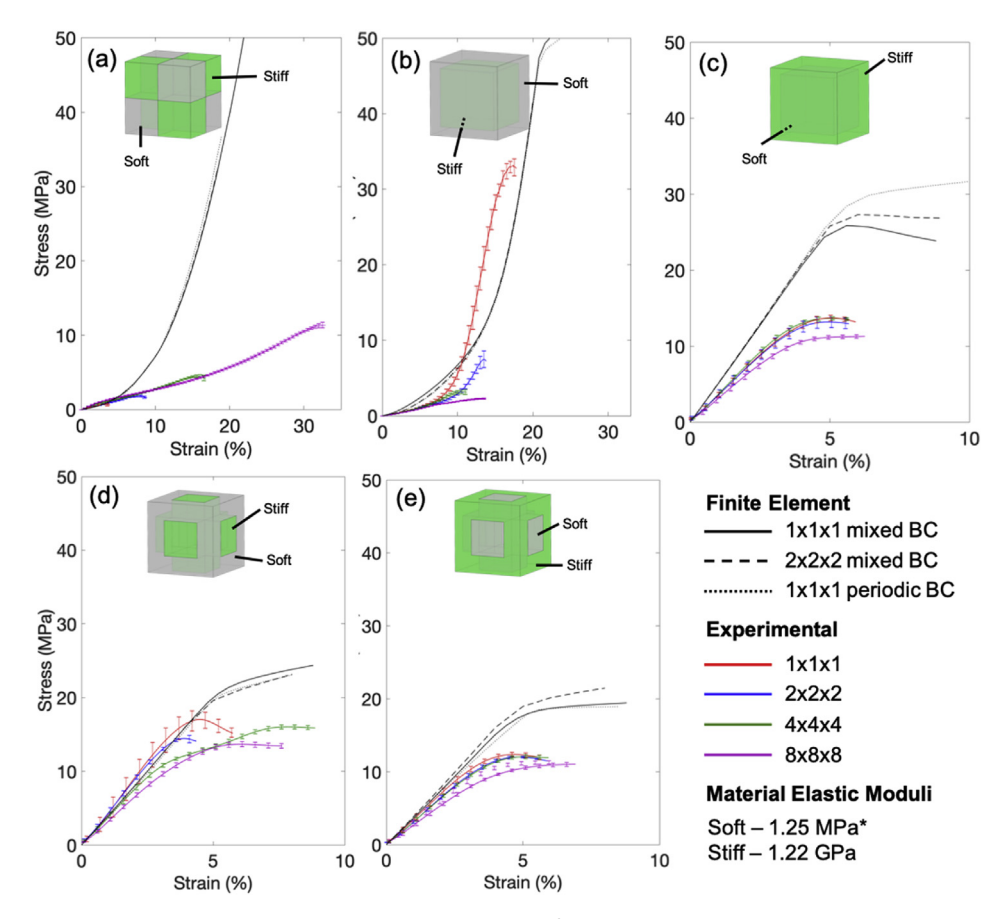


Fig. 2 – Stress-strain curves of 3D printed cubic samples (12.7 mm³) with increasing number of unit cells: (a) discontinuous phase composites, (b) matrix-inclusion composite with soft frame, (c) matrix-inclusion composite with stiff frame, (d) interpenetrating phase composite with stiff frame. The black (solid, dashed, and hashed lines) are results from finite element modeling of each composite type for periodic and mixed boundary conditions (BC). Elastic moduli of the soft and stiff material used for finite element simulations are 1.25 MPa* and 1.22 GPa, respectively. *Indicates linear assumption for the soft material for strains under 10%.

samples with MBCs (which approximate the experimentally applied boundary conditions), PBCs, and a $2 \times 2 \times 2$ sample with MBCs. Behaviors of single-unit cells are described in [28], and average stress-strain curves of unit cells are shown in the Appendix (Fig. A1). In experiments, as the number of unit cells increases, the DPC (Fig. 2a) maintains an almost constant elastic modulus, but its yield strength and correspondingly yield strain increase. The MIC with soft frame single unit cell (Fig. 2b) exhibits a characteristic low stiffness at low strains when the soft frame is deforming, and stiffening as the strain increases due to the load being supported by the direct interaction of stiff inclusions at higher strains. This behavior is visible in the 1 \times 1 \times 1 and 2 \times 2 \times 2 samples, while for 4 \times 4 \times 4 and $8 \times 8 \times 8$ unit cells we do not observe such dramatic stiffening in the stress-strain curves. FE modeling results show this characteristic behavior in the unit cell under both MBCs and PBCs. Finally, for the MIC with a stiff frame and IPC geometries (Fig. 2c, d, and e), the stiffness decreases as the number of unit cells increases.

Scale effects have been studied for cellular solids [35-40]. A theoretical study found that as scale increases, moduli increase in ductile cellular materials under uniaxial compression and simple shear [35]. In experiments, the modulus was found to increase to a plateau when $L/d\approx 6$, where L is the specimen size, and d is cell size; strength also increased with an increased number of unit cells [36]. An experimental study on triply periodic cellular solids concluded that a cubic sample length of five unit cells was sufficient to measure effective mechanical properties [37]. Abueidda et al. [38] showed that depending on the applied strain rate and relative density, samples of 3D printed triply periodic minimal surface architectures with 2x2x2 unit cells have nearly the same mechanical properties as samples with a higher number of unit cells. Our results show that even for samples with up to 8x8x8 unit cells, a larger scale results in the decreased modulus and compressive yield strength. In agreement with our results are the FE findings [39] on cellular solids under direct compression that show that increasing the number of repeated units of a cellular solid in the loading direction results in a decrease in compressive yield strength. However, our material is a filled composite rather than a porous, cellular solid.

In almost every geometry, the FE models predict higher strength and are generally consistent for $1\times1\times1$ and $2\times2\times2$ unit cells regardless of boundary conditions (Fig. 3a). Meanwhile, yield strain (Fig. 3b) is similar for all geometries with a continuous stiff phase (MIC with a stiff frame and IPCs). FE models also generally predict higher elastic moduli for all of the model composites (Fig. 3c). The exceptions to this rule are the DPC and IPC soft frame composites, which have higher elastic moduli but lower yield strengths compared to the FE results. Values for yield strain, yield stress, and elastic modulus obtained experimentally and from FE simulations are given in Table A1 in the Appendix.

Elastic modulus values can also be compared to those estimated from the effective modulus predictions (based on a constant volume fraction of 50% of each phase) of Voigt, Reuss, Voigt—Reuss—Hill, and Hashin-Shtrikman bounds, which are given by equations shown in Table 3. Values in Table 3 were calculated with mechanical properties of the stiff and soft polymers obtained in experiments (a) given in Table

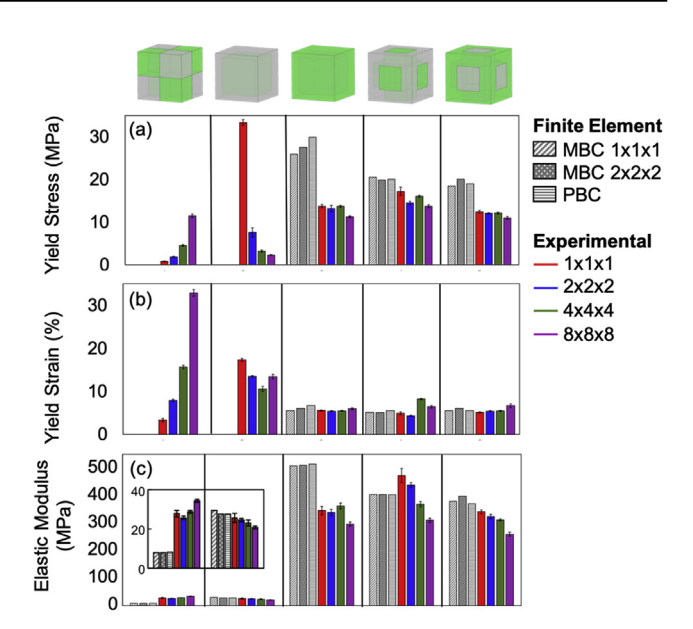


Fig. 3 — (a) Yield strength, (b) yield strain, (c) elastic moduli of composites with a constant sample size and increasing number of cells. Inset in (c) is zoomed in view of elastic modulus for discontinuous phase composite and matrix inclusion composite with soft frame. Finite element modeling results in gray show results using mixed boundary conditions (MBC) or periodic boundary conditions (PBC).

1. Values for elastic modulus obtained from FE simulations are also listed in Table 3 for comparison. For these equations to be used, materials are assumed to be linearly elastic and isotropic. In the case of the soft phase, approximate linear and elastic behavior at strains below 10% were assumed, and a modulus of 1.25 MPa was used, which was measured from mechanical testing by taking the tangent modulus starting at the initial point. As mentioned previously, the anisotropy of Objet PolyJet materials has been shown to be minimal, which is why the isotropic material properties are valid for use [31]. The Voigt and Reuss models overestimate and underestimate the elastic moduli, respectively. However, the Voigt model is much closer to the value of the elastic moduli of the $1 \times 1 \times 1$ IPC composites and the MIC with a stiff frame due to the assumption of constant strain. In contrast, the Reuss model assumes constant stress, making it closer to the behavior of the MIC with a soft frame and stiff inclusions [40]. It is clear from our previous work with these geometries that uniform stress is not present and that the stress is mainly localized in the stiff phase, especially when the stiff phase is continuous [28]. While our composites follow neither uniform strain nor uniform stress assumption, the former is a closer approximation than the latter. This is because the compression platens constrain deformation, whereas internal stresses in each phase are not uniform, as shown in our previous study [28]. The results from Voigt and Reuss models differ significantly due to the large mismatch between properties of the two phases, while the Voigt-Reuss-Hill model provides simple approximations of properties between the two [40].

Table 3 – Effective modulus equations and calculated values based on properties of VeroClear and TangoBlack + with a volume fraction (φ) of 0.5 for each phase. Effective modulus values are estimates for all samples since all samples have 0.5 volume fraction of each phase. Values are calculated with mechanical properties of the stiff and soft polymers obtained in experiments (a) given in Table 1: Elastic modulus (E) values are 1220 MPa and 1.25 MPa for stiff and soft polymer, respectively. Values obtained from FE simulations using the same materials properties are also provided for comparison.

Model Type	Composite type	Effective Modulus (MPa)
Voigt	_	610
Reuss	_	2.5
Voigt-Reuss-Hill	_	306
Hashin-Shtrikman (upper bound)	_	408
Hashin-Shtrikman (lower bound)	_	3.74
FE simulations	Discontinuous phase composite	7.67
	Matrix-inclusion composite (soft frame)	28.4
	Matrix-inclusion composite (stiff frame)	502
	Interpenetrating phase composite (soft frame)	398
	Interpenetrating phase composite (stiff frame)	378

The Hashin-Shtrikman bounds give narrower predictions of effective elastic modulus than the Voigt and Reuss models, as expected [41]. The Voigt–Reuss–Hill and Hashin-Shtrikman upper bound models more closely match the properties observed in experiments for the MIC stiff frame and IPCs elastic moduli since the stiff phase governs. The elastic moduli obtained from FE simulations for all composite types lie between results from Voigt and Reuss models. However, when comparing FE results with the Hashin-Shtrikman model, the elastic modulus of MIC with a stiff frame is higher than the upper Hashin-Shtrikman bound. This may be due to the cubic symmetry of the composites studied here (except for the DPC) while the used Hashin-Shtrikman model was developed for isotropic composites.

Planar (2D) strains were measured using DIC. The DIC results for ε_{xy} , ε_{yy} , and ε_{xx} at the end of the linear region of the stress-strain curve are shown in Fig. A2 and Fig. A3. As previously observed [28], the soft phase contributes more to deformation. The strain component ε_{yy} is highest in the soft phase while the highest ε_{xy} strain is at the interface between the stiff and soft phase. The deformations of samples after compression until the end of the linear region of the stress-strain curve are shown in Fig. 4. Arrows show the locations where the soft phase is deformed. Starting with the DPC, it can be seen that the soft phase undergoes compression, while the stiff polymer regions generally stay relatively uncompressed. Such deformation leads to eventual debonding between the laterally adjacent stiff and soft units since the corners between phases cannot stay joined when only the soft phase deforms. This is most visible in the $1 \times 1 \times 1$ and $2 \times 2 \times 1$ 2 samples. Outward deformation of the soft phase can be seen (pointed to by arrows) and is corroborated by the high shear strain seen in DIC results (Fig. A2). As the number of unit cells increases, it appears that the strain is more distributed throughout the whole sample, leading to larger overall yield strains as the platen can be seen compressing the sample more for $4 \times 4 \times 4$ and $8 \times 8 \times 8$ samples to reach yield strain.

For the MIC soft frame, the strain is localized in the soft phase as the number of unit cells increases. The strain localization develops in regions in between the stiff inclusions and leads to buckling of the sample during compression, which is visible in the $4 \times 4 \times 4$ and $8 \times 8 \times 8$ samples (Fig. 4). In the DIC results (Fig. A2), shear strains are localized in the regions

between the stiff inclusions in the $2 \times 2 \times 2$ and $4 \times 4 \times 4$ samples. Additionally, sample buckling results in the overall shear deformation between the top and bottom halves of the $8 \times 8 \times 8$ sample as can be seen by the red and blue coloration. Strain localizations have less effect on overall material stability when there is a continuous stiff phase. This behavior is seen in the MIC with a stiff frame and both IPC-types. For the MIC with a stiff frame, buckling of the stiff phase can be seen at the lateral walls of the material. As the soft phase deforms, it pushes the thin walls at the edges of the samples outwards. In both IPCs, the load is carried by the stiff phase, so the compression of the soft phase and restriction from the stiff phase causes the soft phase to deform where it can on the outer surfaces. This behavior was also seen in our previous FE modeling results [28].

While 3D printing has been used extensively to study composites and their behaviors, the influence of interface properties and thickness has not been studied in-depth, as interfaces are generally assumed to be perfectly bonded. Dimas et al. [5] made the assumption of perfect bonding after observing that the interface adherence was stronger than the strength of the soft phase. However, this interfacial behavior may be due to the soft phase's small dimensions in their study, which was only 250 µm wide. They mention that certain topologies were not synthesized well using the printing process due to the small dimensions of the print and that mixing likely occurs at the interfaces between the different materials in the composite. With the AM method used, which is the same as what is used in the current study, mixing of materials at the interface is inevitable, and the influence of these mixing or printing imperfections at the interface is magnified as feature sizes become small. The interface surface-area-to-sample-volume ratio increases as the number of unit cells is increased, while keeping the overall sample size the same. These values were calculated for our sample size and are shown in Table 2. These results show that for a 12.7 \times $12.7\times\,12.7~\text{mm}^3$ sample size, we expect the stiffness of the DPC to drop the most between the $1 \times 1 \times 1$ and $8 \times 8 \times 8$ since the surface area-to-sample volume ratio increases the most. The MIC and finally the IPC come next in this expected behavior based on their surface area-to-sample ratio. The exact opposite trend is observed in Fig. 3, where the DPC stiffness increases slightly with the number of unit cells, MICs

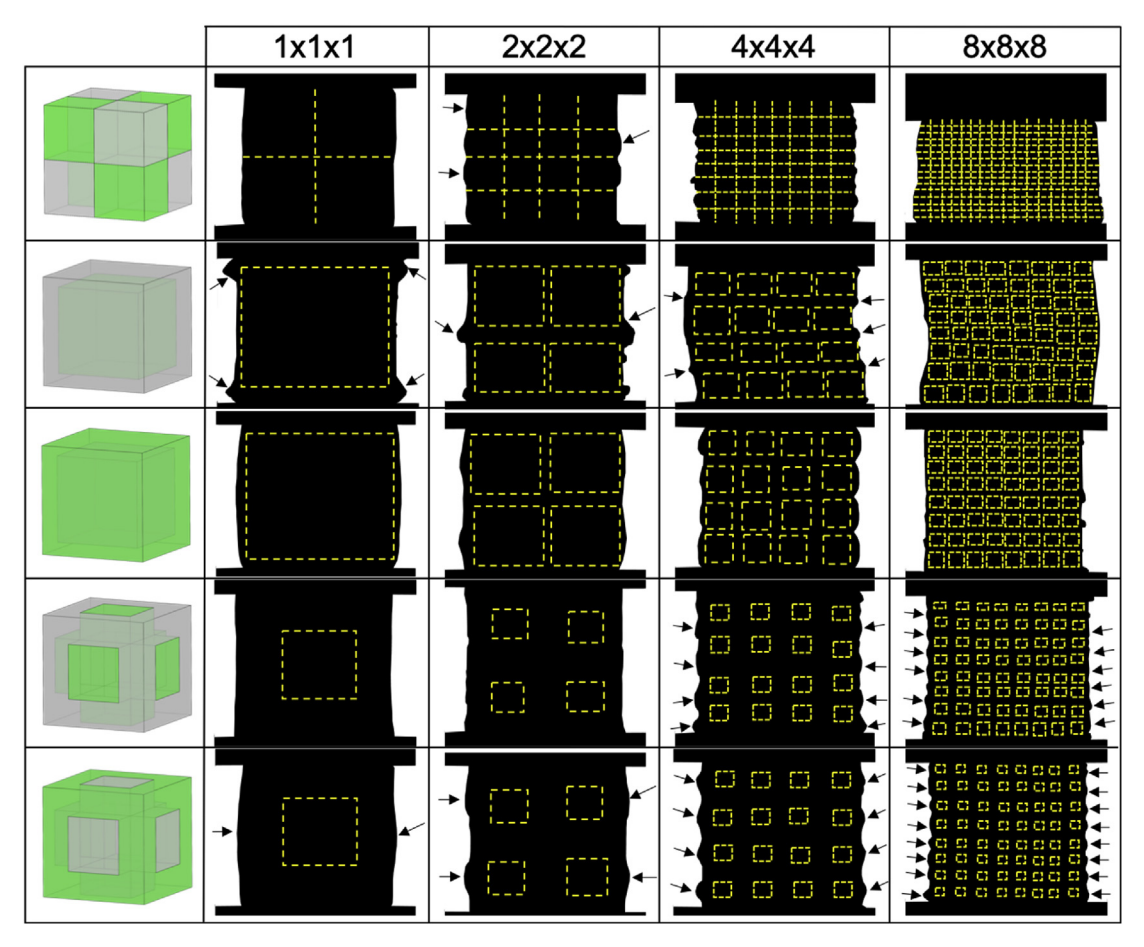


Fig. 4 – Deformation of cubic samples (12.7 mm³) with different numbers of unit cells ($1 \times 1 \times 1$, $2 \times 2 \times 2$, $4 \times 4 \times 4$, and $8 \times 8 \times 8$) at the yield strains for the respective sample types. From top to bottom (gray = soft, green = stiff): discontinuous phase composite, matrix-inclusion composite with soft and stiff frames, and interpenetrating phase composite with soft and stiff frames. Background was removed and samples were colored using Adobe Photoshop to make deformation more visible. Yellow dotted lines are approximate locations of boundaries between phases shown for single unit cells. Arrows point to regions of soft phase deformation.

have a slightly decreasing trend, and IPCs decrease in stiffness the most with the number of unit cells. This behavior of DPC may be due to the lack of a continuous phase to transmit loads.

The perfect bonding assumption was not found to be valid for DPC through observations of the composite materials during experiments. The debonding can be seen most easily in the DPC $1\times1\times1$ composite at the corner region between the phases, where there is a high shear strain, as shown in DIC results (Fig. A2). Other composite types did not exhibit such visible debonding behavior, as confirmed by FE simulations. Assuming perfectly bonded interfaces compared with free slippage at interfaces did not result in significant changes in overall modulus or maximum obtainable stress.

The scale effects show that increasing the number of unit cells decreases material properties for most composite types. In this experimental set, as the scale is increased, the individual unit cell size is decreased. We also explored size effects to understand the effect of only decreasing unit cell size, as discussed in the next section.

3.2. Size effects: decreasing size of a unit cell for a single cell

The second set of samples (set (b)) involved testing individual unit cells of different sizes to provide insights on the size effects in 3D printed composites. Fig. 5 shows the average curves for each composite type related to size, and analysis was done for specimens of the component materials (Fig. 5a-b) and the composites (Fig. 5c-g).

Starting with the single-phase samples and based on general materials concepts, it is expected that the elastic modulus remains the same while the strength increases when the sample size decreases. Previous studies on brittle materials, such as ceramics and crystalline polymers, have shown that strength increases because of the probability that defects are present in a material decreases as the sample size decreases, both in tension and compression testing [40,42–45]. The effect of sample size has not been studied for additively

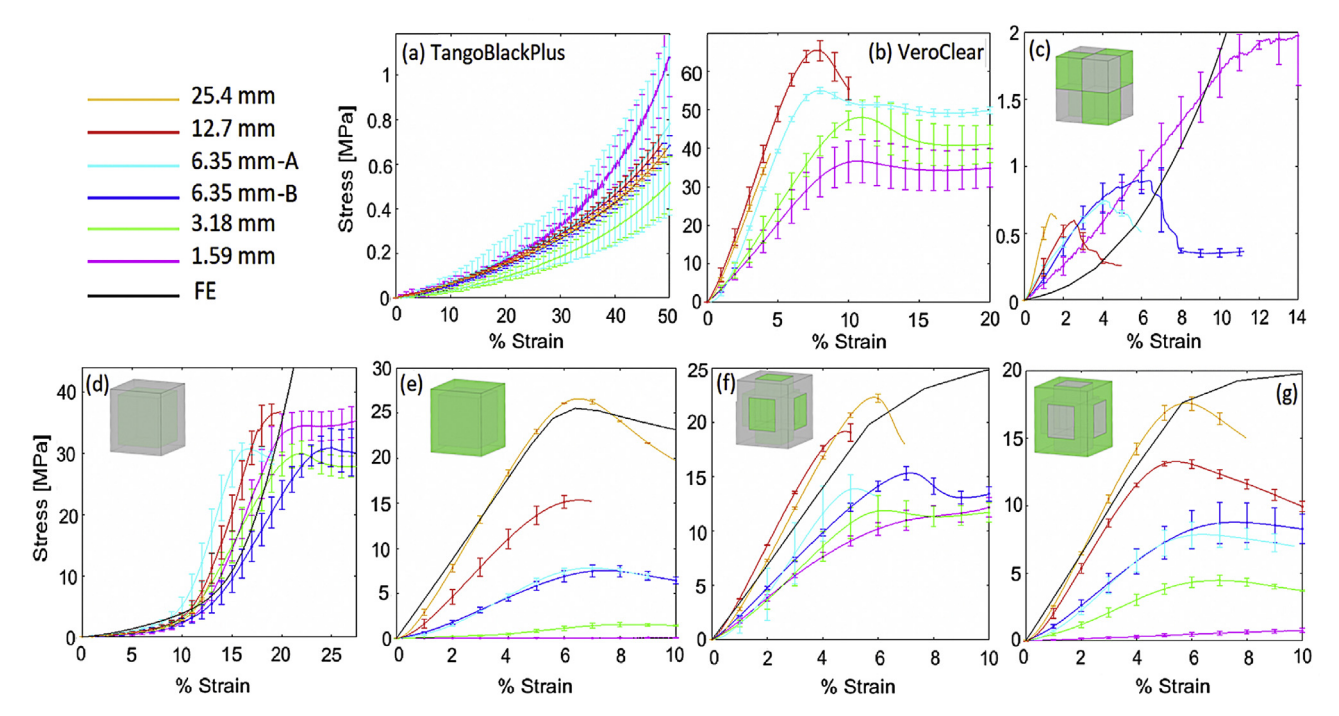


Fig. 5 – Average stress–strain curves for $1 \times 1 \times 1$ samples with different sizes. Component materials (a) soft phase material (TangoBlack +) and (b) stiff phase material (VeroClear), and composite geometries (c) discontinuous phase composite, (d) matrix-inclusion composite with soft frame, (e) matrix-inclusion composite with stiff frame, (f) interpenetrating phase composite with soft frame, and (g) interpenetrating phase composite with stiff frame are shown.

manufactured composites. Also, size effects are still poorly understood across different printing techniques for a single material [45-48]. The homogeneous stiff and soft materials stress-strain curves are shown in Fig. 5a, b. The nonlinear soft material (TangoBlack +) shows no significant size effect. For the stiff polymer (VeroClear), the elastic modulus and strength decrease as the sample size decreases. An opposite trend is seen in the literature for traditional brittle materials. However, our results agree with [46], where size effect was studied for additively manufactured stainless steel tested under tension. On the other hand, Bell and Siegmund [45] report a nonmonotonical dependence of strength on the size of 3D printed polymer tested under bending. The change in stiffness may imply that the print's microstructure at small dimensions is different (e.g., print layer thickness to sample size ratio), resulting in a decreased elastic modulus [45].

For all composites, the elastic moduli of unit cells decrease as the sample size decreases, which is counterintuitive given that elastic modulus is a material constant and thus should be independent of specimen size. Possible reasons for changes in elastic modulus with size include: 1) an increase in UV exposure in the smaller samples (since the specimens were all printed during the same batch, small samples could receive more UV exposure to the whole part while taller prints were being completed during the print) and 2) increased hydration in larger samples after the specimens were rinsed of support material and not enough time passed for drying between rinsing and mechanical testing. An increase in stiffness after UV exposure has been documented in the literature [49]. However, the above reasons would imply that the smaller

samples should show an increase in elastic modulus, which is the opposite of what was observed in mechanical testing. Alternatively, the use of support material surrounding the sample has been suggested to have a UV-shielding effect on 3D printed samples printed with RGD240, preventing it from fully curing [49]. Since the samples in this study were printed in the matte mode, which deposits support material on all sides of the print, it is possible that the UV-shielding effect would be more pronounced in smaller samples. In small samples, the laterally deposited support material may shield most of the sample. Conversely, the centers of the larger prints are farther from the support material and may therefore cure more, resulting in larger samples being stiffer.

Another reason could be that the layer-by-layer printing of the samples leads to surface defects, which influence the elastic modulus. A decrease in elastic moduli of bone (when assumed to be effectively homogenous) [50] as the size decreased was reported. The explanation provided was that this behavior was the result of material surface state, where a surface that is rough and more compliant than the bulk material can lead to lower stiffness [51]. In Fig. A5a, optical microscopy results show that the VeroClear samples have a layered microstructure at the surface. Fig. A5b and c show that these layers are aggregates of even thinner layers. While the exact thickness of the thinnest layers could not be resolved from the microscope images, they appear to be ~20 μm, which is similar to the 30 µm layer thickness reported by the manufacturer. Measurements of the aggregate layers for each imaged sample are summarized in Table A3. They show that the average aggregate layer thickness of VeroClear varies

from 95 to 375 µm with large standard deviations within sample. The aggregate layer thickness TangoBlack + appears to be smaller (\sim 60 μ m). However, a comprehensive study should be done in the future to examine the variation in aggregate layer thickness across all samples, including the composite prints. The surface layer, constant in thickness, would be larger by volume in smaller samples. Besides, the larger aggregate layer thicknesses in VeroClear may help explain why VeroClear shows a more pronounced change in modulus compared to VeroClear. The composite samples with VeroClear at the surface (Fig. 5e, g) also show a larger decrease in modulus. This observation leads us to conjecture that the softening in the 3D printed composites in the current study may be due to printing defects at the surface or interfaces of samples.

Strength was found to decrease with the smaller sample size. This trend is especially pronounced in the MIC and IPC samples with stiff continuous outer phases. The elastic modulus dropped dramatically for the aforementioned composite types when transitioning from 3.18 mm to 1.58 mm edge length (Fig. 6). As the sample becomes small, the thickness of the outer phase becomes very small, and any printing defects on the surface of the unit cell likely have a large effect. In comparison, the MIC and IPC with a soft frame show lower drop-offs in strength and stiffness. The central column in the IPC with a soft frame likely helps maintain strength and stiffness. DPCs show that the strength increases when the unit cell size decreases, which is similar to what is seen in DPC when the number of unit cells increases. Values for yield stress and elastic modulus from experimental and FE simulations are listed in Table A2 in the Appendix.

Thus, experiments (a) and (b) show similar trends. The decreases in stiffness and strength are seen when increasing scale (decreasing unit cell size while keeping the same sample

size) or decreasing the unit cell size for samples with a single unit cell. The main factors giving this trend are likely to be imperfections on the surfaces of prints and the microstructures of the samples, including the print layer to the size of a unit cell ratio [45].

4. Conclusions

Inspired by biological composite materials consisting of stiff and soft phases arranged in different architectures, five geometries of two-phase polymer composites were tested to understand scale and size effects on mechanical properties of 3D printed composites: a discontinuous phase composite (DPC), a matrix-inclusion composite (MIC) with a stiff frame and one with a soft frame, and interpenetrating phase composites (IPC) with either a stiff or a soft frame. Two types of comparison tests were performed: (a) increase the number of unit cells while keeping the overall sample size the same, which effectively decreases the unit cell size, and (b) increase the sample size where only one unit cell is present.

Key findings are listed below and summarized in Table 4:

- Yield strength and elastic modulus generally decrease as unit cell size decreases except of the yield strength for DPC.
 Both elastic modulus and yield strength for MIC with a soft frame do not show significant size effects.
- While the strain is higher in the soft phase and localization of strain is observed from DIC and sample deformation after compression in all samples, strain localization in the matrix-inclusion composite with a soft frame leads to overall material instability and sample bending for $4 \times 4 \times 4$ and $8 \times 8 \times 8$ samples.

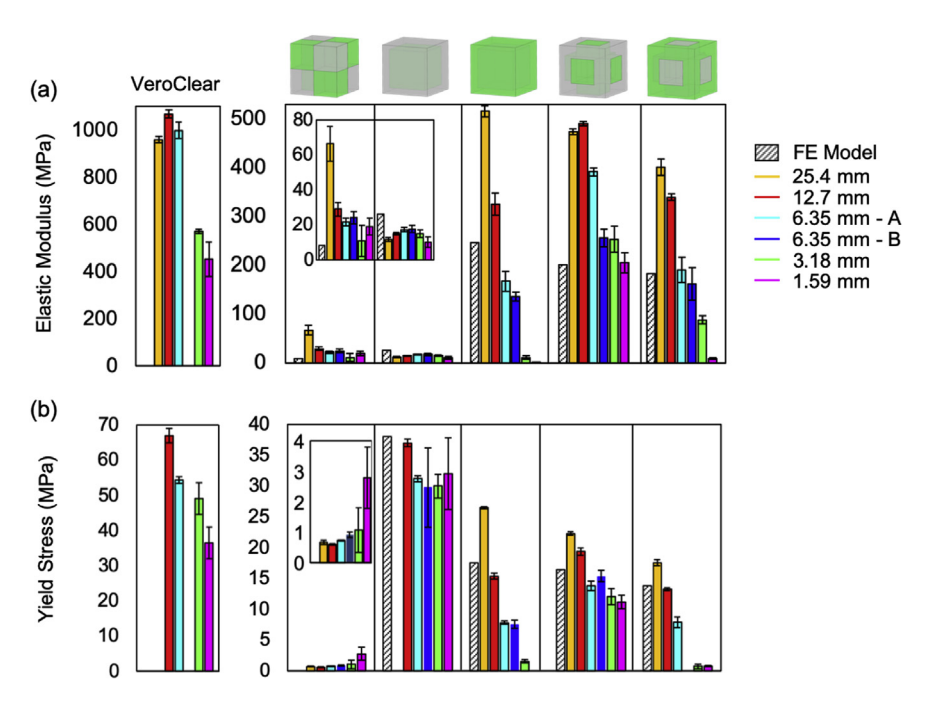


Fig. 6 – (a) Elastic moduli, and (b) yield stress of composites with decreasing unit cell size.

Table 4 – Summary of trends in elastic modulus and compressive yield strength in the homogeneous materials and composite types shown in this study. Arrows indicate increases (\uparrow) or decreases (\downarrow) in mechanical property values as scale increases or size decreases. The numbers in parentheses indicate the percentage of change in mechanical property values between 1 \times 1 and 8 \times 8 \times 8 samples for scale effects, and sample size 1.59 mm and 25.4 mm for size effects.

Material Type		Mechanical Property	Scale ↑	Size ↓
TangoBlack+		Stiffness	_	_
		Compressive Yield Strength	_	_
VeroClear		Elastic Modulus	_	↓ (52.8%)
		Compressive Yield Strength	_	↓ (NA)
Discontinuous Phase Composite	_	Elastic Modulus	↑ (23.3%)	↓ (71.3%)
		Compressive Yield Strength	↑ (1362.0%)	_
Matrix Inclusion Composite	Soft frame	Elastic Modulus	↓ (20.0%)	_
		Compressive Yield Strength	↓ (93.1%)	_
	Stiff frame	Elastic Modulus	↓ (14.5%)	↓ (99.8%)
		Compressive Yield Strength	↓ (18.2%)	↓ (NA)
Interpenetrating Phase Composite	Soft frame	Elastic Modulus	↓ (34.5%)	↓ (56.7%)
		Compressive Yield Strength	↓ (20.3%)	↓ (49.8%)
	Stiff frame	Elastic Modulus	↓ (23.7%)	↓ (97.8%)
		Compressive Yield Strength	↓ (11.3%)	↓ (95.8%)

- ullet FE models generally predict higher strengths and elastic moduli than experimental results for experiments (a) and are consistent for 1 \times 1 \times 1 and 2 \times 2 \times 2 unit cells regardless of boundary conditions. DPC and IPC soft frame composites have higher elastic moduli but lower strengths compared to FE results.
- The Voigt-Reuss-Hill and Hashin-Shtrikman upper bound models predict an elastic modulus close to those of composites with a continuous stiff frame (the MIC stiff frame and IPCs), while the Hashin-Shtrikman lower bound is closest to (but underestimates) the moduli of the DPC and MIC with soft frame.
- In general, smaller 3D printed composites have lower strength and elastic modulus. Imperfections from the 3D printing process, such as the larger print ratio of layer thickness to the overall sample size for smaller samples, mixing at material interfaces, and UV-shielding effects from the support material when printed in "matte mode", are likely the cause of these results.

This research provides a foundation for more comprehensive studies of the scale and size effects on mechanical properties of 3D printed composites.

Declaration of Competing Interest

The authors declare that they have no known competing financial interests or personal relationships that could have appeared to influence the work reported in this paper.

Acknowledgements

This work was supported by the National Science Foundation Biomaterials program, grants DMR-1507978 and DMR-

1507169, and Mechanics of Materials and Structures program grants 1926353 and 1926361. This research was carried out in part in the Materials Research Laboratory Central Research Facilities, University of Illinois. The authors would also like to thank researchers at the University of California at San-Diego: Benjamin Shih and Chris Cassidy for coordinating and assisting with 3D printing; Andrei Pissarenko for guidance on digital image correlation; Professor Vlado Lubarda for feedback and discussion on the Voigt, Reuss, and Hashin-Shtrikman models; Dr. Julio Soares at the University of Illinois for optical microscopy of printed samples; and Rachel Hsiong for collection of preliminary data.

Appendix A

3D Print Material Density

The printed samples had an average density ranging from $1.058~g/cm^3$ to $1.075~g/cm^3$ with an average density of $1.070\pm0.003~g/cm^3$. The pure material average densities were found to be $1.10~g/cm^3$ for VeroClear and $1.06~g/cm^3$ for TangoBlack+. Different dimensions were also measured depending on the direction of printing as also observed from other studies [53]. The height of the samples, which is the dimension perpendicular to the printing plane, is shorter than the two dimensions parallel to the printing plane. Generally, the height was more dimensionally accurate than the width and thickness dimensions of 3D printed composites. An increase in deviation from original computer-aided design dimensions occurred as printed sample size decreased.

Table A1 - Yield strain, yield stress, and elastic modulus values from finite element (FE) simulations and experiments (a). Values for experiments are given as average (s.d.) and n=6 for each sample type. FE results include those using mixed boundary conditions (MBC) or periodic boundary conditions (PBC).

Network type	Condition	Sample type	Yield Strain (%)	Yield Stress (MPa)	Elastic Modulus (MPa)
Discontinuous phase composite	FE MBC	1 × 1 × 1	_	_	7.79
	FE MBC	$2 \times 2 \times 2$	_	_	7.98
	FE PBC	_	_	-	8.02
	Experiment	$1\times1\times1$	3.3 (0.4)	0.78 (0.05)	27.9 (1.7)
	•	$2 \times 2 \times 2$	7.9 (0.3)	1.87 (0.12)	25.67 (0.9)
		$4 \times 4 \times 4$	15.6 (0.4)	4.51 (0.18)	28.7 (0.8)
		$8 \times 8 \times 8$	32.9 (0.8)	11.4 (0.4)	34.4 (0.8)
Matrix-inclusion composite (soft frame)	FE MBC	$1 \times 1 \times 1$	- ` ′	- ` ′	29.60
• • • •	FE MBC	$2 \times 2 \times 2$	_	_	27.80
	FE PBC	_	_	_	27.80
	Experiment	$1 \times 1 \times 1$	17.3 (0.4)	33.3 (0.6)	26 (2)
	•	$2 \times 2 \times 2$	13.5 (0.2)	7.6 (1.1)	24.5 (0.9)
		$4 \times 4 \times 4$	10.6 (0.6)	3.2 (0.3)	23.1 (1.5)
		$8 \times 8 \times 8$	13.4 (0.5)	2.3 (0.1)	20.8 (0.8)
Matrix-inclusion composite (stiff frame)	FE MBC	$1 \times 1 \times 1$	5.5	25.88	507.7
· · · · · ·	FE MBC	$2 \times 2 \times 2$	6	27.5	509.8
	FE PBC	_	6.7	29.87	514.3
	Experiment	$1 \times 1 \times 1$	5.54 (0.12)	13.7 (0.4)	346 (15)
	•	$2 \times 2 \times 2$	5.35 (0.12)	13.2 (0.7)	338 (12)
		$4 \times 4 \times 4$	5.45 (0.10)	13.7 (0.2)	363 (11)
		$8 \times 8 \times 8$	5.9 (0.2)	11.2 (0.2)	296 (8)
Interpenetrating phase composite (soft	FE MBC	$1 \times 1 \times 1$	5.1	20.5	403.8
frame)	FE MBC	$2 \times 2 \times 2$	5	19.8	403.8
•	FE PBC	_	5.5	20	403
	Experiment	$1 \times 1 \times 1$	4.9 (0.3)	17.2 (1.0)	472 (26)
	•	$2 \times 2 \times 2$	4.31 (0.15)	14.5 (0.4)	439 (8)
		$4 \times 4 \times 4$	8.20 (0.16)	16.0 (0.3)	369 (9)
		$8 \times 8 \times 8$	6.4 (0.3)	13.7 (0.4)	309 (8)
Interpenetrating phase composite (stiff	FE MBC	$1 \times 1 \times 1$	5.5	18.42	379
frame)	FE MBC	$2 \times 2 \times 2$	6	20	398.1
	FE PBC	_	5.5	18.94	370.2
	Experiment	$1 \times 1 \times 1$	5.09 (0.12)	12.4 (0.3)	341 (7)
	•	$2 \times 2 \times 2$	5.36 (0.14)	12.04 (0.14)	323 (8)
		$4\times4\times4$	5.5 (0.1)	12.1 (0.2)	312 (4)
		$8 \times 8 \times 8$	6.7 (0.4)	11.0 (0.3)	260 (7)

Table A2 – Yield stress and elastic modulus of $1 \times 1 \times 1$ samples with different unit cell size obtained from experiments (b) and finite element modeling. Values for experiments are given as average (s.d) and n=3 for each sample type.

Sample type	Condition	Sample size (mm)	Yield stress (MPa)	Elastic Modulus (MPa)
Discontinuous phase composite	FE	-	-	8.09
	Experiment	1.59 mm	2.79 (1.01)	19.1 (4.8)
		3.18 mm	1.06 (0.74)	10.9 (8.9)
		6.35 mm-B	0.91 (0.09)	24.2 (3.6)
		6.35 mm-A	0.74 (0.00)	21.8 (2.3)
		12.7 mm	0.60 (0.02)	29.0 (4.1)
		25.4 mm	0.67 (0.06)	66.5 (9.9)
Matrix-inclusion composite (soft frame) ^a	FE	_	38.1	26.2
	Experiment	1.59 mm	32.8 (5.8)	10.1 (3.1)
		3.18 mm	30.0 (1.9)	14.9 (2.1)
		6.35 mm-B	29.8 (6.4)	17.7 (2.2)
		6.35 mm-A	31.2 (0.5)	17.3 (1.2)
		12.7 mm	37.0 (0.6)	14.8 (0.7)
		25.4 mm	_	11.6 (1.0)
Matrix-inclusion composite (stiff frame)	FE	-	17.5	246
	Experiment	1.59 mm	-	0.93 (0.46)
		3.18 mm	1.58 (0.29)	10.6 (3.5)
		6.35 mm-B	7.56 (0.66)	136 (9)
		6.35 mm-A	7.83 (0.28)	167 (20)
		12.7 mm	15.4 (0.5)	325 (23)
		25.4 mm	26.5 (0.2)	515 (11)
Interpenetrating phase composite (soft	FE	-	16.4	201
frame)	Experiment	1.59 mm	11.2 (1.1)	205 (20)
		3.18 mm	12.1 (1.3)	253 (27)
		6.35 mm-B	15.4 (0.9)	255 (18)
		6.35 mm-A	13.8 (0.8)	391 (8)
		12.7 mm	19.4 (0.6)	490 (5)
		25.4 mm	22.3 (0.3)	473 (6)
Interpenetrating phase composite (stiff	FE	-	13.8	183
frame)	Experiment	1.59 mm	0.74 (0.10)	9.00 (1.80)
		3.18 mm	4.50 (0.39)	88.0 (8.0)
		6.35 mm-B	8.80 (1.50)	162 (33)
		6.35 mm-A	7.90 (0.93)	190 (26)
		12.7 mm	13.3 (0.2)	339 (7)
		25.4 mm	17.6 (0.5)	401 (17)

^a Modulus values reported for MIC-soft samples are calculated based on the initial linear region in stress-strain curves.

Table A3 - Aggregate layer thicknesses and standard deviations of VeroClear and TangoBlack + calculated from optical microscope results. N represents the number of measurements taken per sample.

Sample and Size	Aggregate Layer Thickness (μm)	Standard Deviation (μm)	N
VeroClear (25.4 mm)	202	110	65
VeroClear (12.7 mm)	105	44	93
VeroClear (6.35 mm)	375	254	20
VeroClear (3.2 mm)	104	39	22
VeroClear (1.58 mm)	95	44	13
TangoBlack+(6.35 mm)	60	31	38
	c · 1 ··	11 C -1 1:CC	

Average stress—strain curves for single unit cells of the different composite types discussed in this paper are shown in Fig. A1.

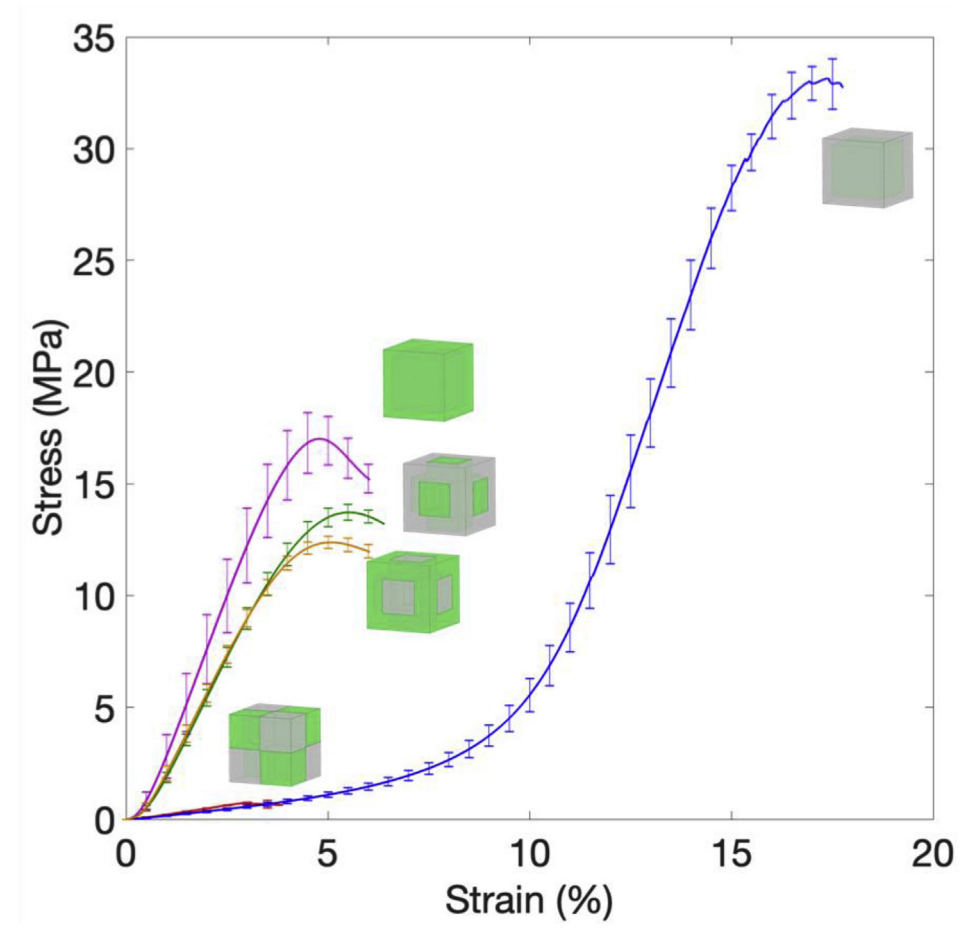


Fig. A1 – Average stress–strain curves of composite unit cells with 12.7 mm edge length. Gray = soft phase, green = stiff phase [21]. Strain maps of ε_{xy} , ε_{yy} , and ε_{xx} from digital image correlation are shown in Figs A2-4.

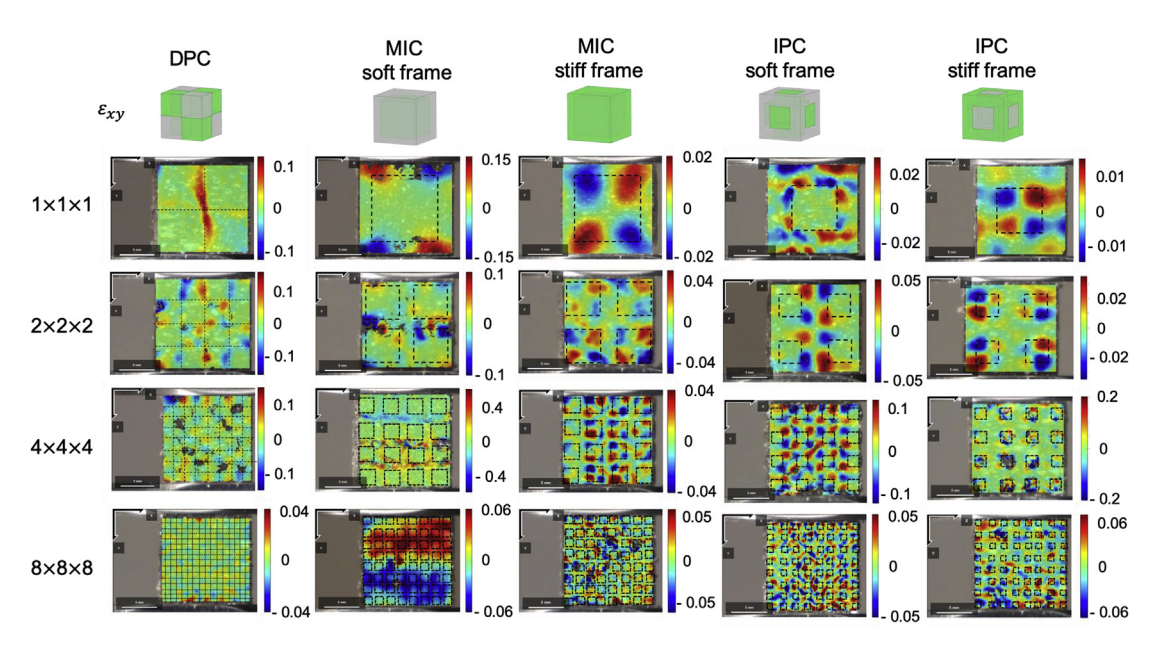


Fig. A2 — Strain maps for ε_{xy} for each composite geometry at the yield strains for the respective sample's types. Boundaries between phases are outlined with black dotted lines.

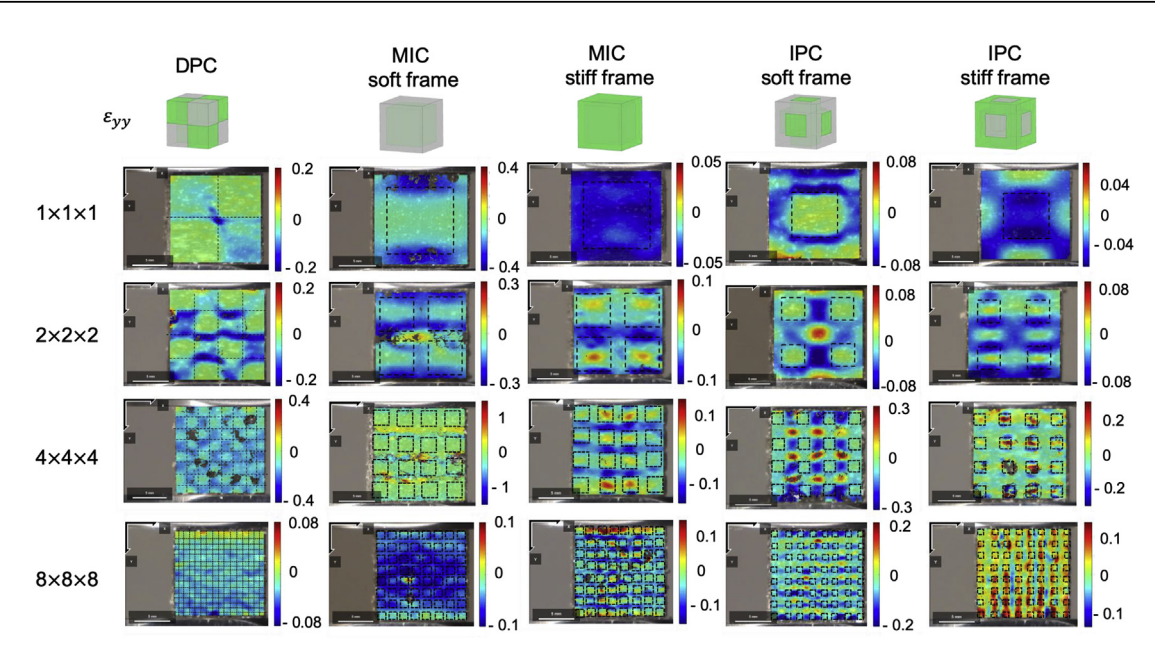


Fig. A3 — Strain maps for ε_{yy} for each composite geometry at the yield strains for the respective sample's types. Boundaries between phases are outlined with black dotted lines.

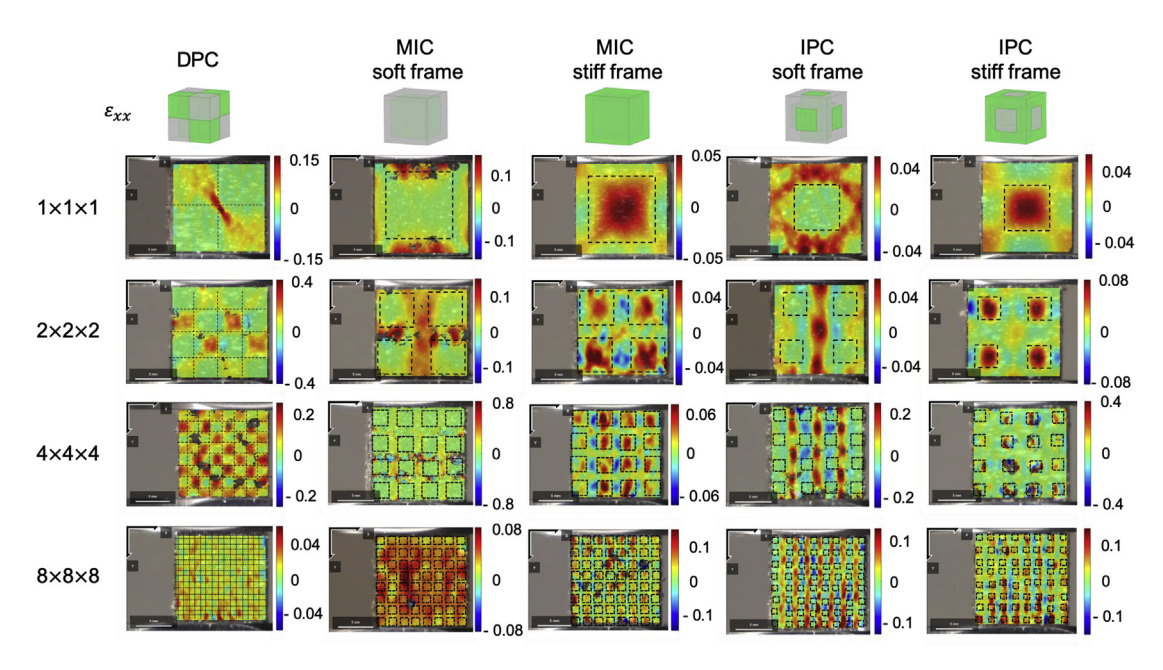


Fig. A4 – Strain maps for ε_{xx} for each composite geometry at the yield strains for the respective sample's types. Boundaries between phases are outlined with black dotted lines. Optical microscopy images are shown in Fig. A5 and the thicknesses of the aggregate layers are summarized in Table A3.

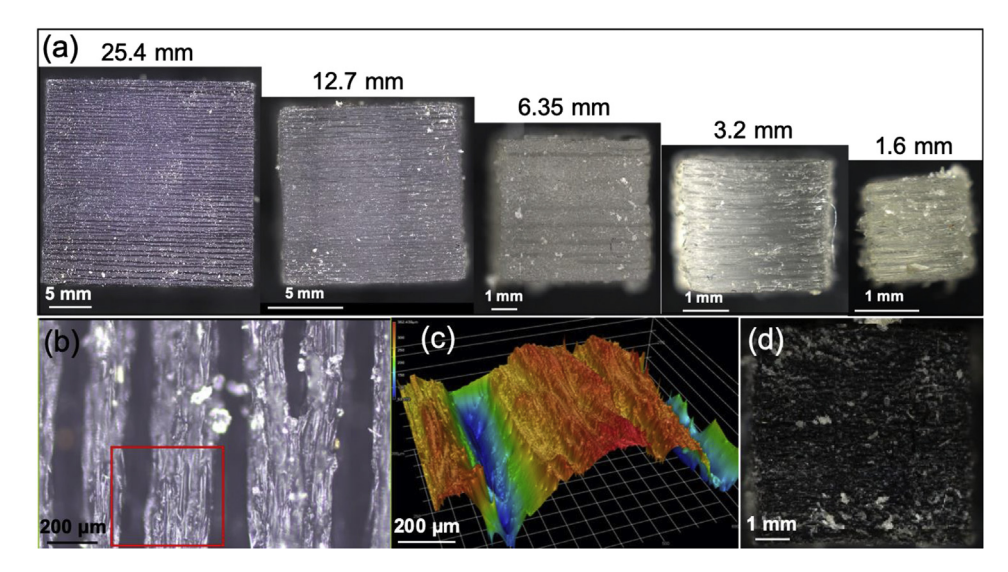


Fig. A5 — (a) Optical microscope images of VeroClear of different sizes (25.4 mm, 12.7 mm, 6.35 mm, 3.2 mm, and 1.6 mm), (b) magnified image of 25.4 mm sample showing aggregate lamellae, (c) a 3D image of surface profile the region shown in red square in (b), and (d) optical microscope image of 6.35 mm edge length TangoBlack+.

REFERENCES

- [1] Jasiuk I, Abueidda DW, Kozuch C, Pang SY, Su FY, McKittrick J. An overview on additive manufacturing of polymers. JOM 2018;70(3):275–83. https://doi.org/10.1007/ s11837-017-2730-y.
- [2] Wickramasinghe S, Do T, Tran P. FDM-Based 3D printing of polymer and associated composite: a review on mechanical properties, defects and treatments. Polym Rev 2020;12(7):1–42. https://doi.org/10.3390/polym12071529. Art no. 1529.
- [3] Porter MM, Adriaens D, Hatton RL, Meyers MA, McKittrick J. Why the seahorse tail is square. Science 2015;349(6243). https://doi.org/10.1126/science.aaa6683.
- [4] Frank MB, Naleway SE, Wirth TS, Jung JY, Cheung CL, Loera FB, et al. A protocol for bioinspired design: a ground sampler based on sea urchin jaws. JoVE 2016;110. e53554e53554.
- [5] Dimas LS, Bratzel GH, Eylon I, Buehler MJ. Tough composites inspired by mineralized natural materials: computation, 3D printing, and testing. Adv Funct Mater 2013;23(36):4629–38.
- [6] Libonati F, Gu GX, Qin Z, Vergani L, Buehler MJ. Bone-inspired materials by design: toughness amplification observed using 3D printing and testing. Adv Eng Mater 2016;18(8):1354–63.
- [7] Gu GX, Takaffoli M, Hsieh AJ, Buehler MJ. Biomimetic additive manufactured polymer composites for improved impact resistance. Extreme Mechanics Letters 2016;9:317–23.
- [8] Zhang P, Heyne MA, To AC. Biomimetic staggered composites with highly enhanced energy dissipation: modeling, 3D printing, and testing. J Mech Phys Solid 2015;83:285–300.
- [9] Gu GX, Takaffoli M, Buehler MJ. Hierarchically enhanced impact resistance of bioinspired composites. Adv Mater Jul 26 2017;29(28). https://doi.org/10.1002/adma.201700060.
- [10] Kumar K, Liu J, Christianson C, Ali M, Tolley MT, Aizenberg J, et al. A biologically inspired, functionally graded end effector for soft robotics applications. Soft Robot 2017;4(4):317–23. https://doi.org/10.1089/soro.2017.0002.

- [11] Bartlett NW, Tolley MT, Overvelde JT, Weaver JC, Mosadegh B, Bertoldi K, et al. A 3D-printed, functionally graded soft robot powered by combustion. Science 2015;349(6244):161-5. https://doi.org/10.1126/ science.aab0129.
- [12] Lin E, Li Y, Ortiz C, Boyce MC. 3D printed, bio-inspired prototypes and analytical models for structured suture interfaces with geometrically-tuned deformation and failure behavior. J Mech Phys Solid 2014;73:166–82.
- [13] Lin E, Li Y, Weaver JC, Ortiz C, Boyce MC. Tunability and enhancement of mechanical behavior with additively manufactured bio-inspired hierarchical suture interfaces. J Mater Res 2014;29(17):1867-75.
- [14] Wang B, Sullivan TN, Pissarenko A, Zaheri A, Espinosa HD, Meyers MA. Lessons from the ocean: whale baleen fracture resistance. Adv Mater 2018:1804574.
- [15] Suksangpanya N, Yaraghi NA, Pipes RB, Kisailus D, Zavattieri P. Crack twisting and toughening strategies in Bouligand architectures. Int J Solid Struct Oct 1 2018;150:83–106. https://doi.org/10.1016/ j.ijsolstr.2018.06.004.
- [16] Velasco-Hogan A, Xu J, Meyers MA. Additive manufacturing as a method to design and optimize bioinspired structures. Adv Mater 2018:1800940. https://doi.org/10.1002/ adma.201800940.
- [17] Cho H, Weaver JC, Pöselt E, in't Veld PJ, Boyce MC, Rutledge GC. Engineering the mechanics of heterogeneous soft crystals. Adv Funct Mater 2016;26(38):6938–49.
- [18] Gu GX, Libonati F, Wettermark SD, Buehler MJ. Printing nature: unraveling the role of nacre's mineral bridges. J. Mech. Behav. Biomed. Mater. Dec 2017;76:135–44. https://doi.org/10.1016/j.jmbbm.2017.05.007.
- [19] Yap YL, Wang C, Sing SL, Dikshit V, Yeong WY, Wei J. Material jetting additive manufacturing: an experimental study using designed metrological benchmarks. no. Supplement C Precis Eng 2017;50:275–85. https://doi.org/ 10.1016/j.precisioneng.2017.05.015. 2017/10/01/.
- [20] Slesarenko V, Rudykh S. Towards mechanical characterization of soft digital materials for multimaterial 3D-printing. Int J Eng Sci Feb 2018;123:62-72. https://doi.org/ 10.1016/j.ijengsci.2017.11.011.

- [21] Bass L, Meisel NA, Williams CB. Exploring variability of orientation and aging effects in material properties of multimaterial jetting parts. Rapid Prototyp J 2016;22(5):826–34. https://doi.org/10.1108/Rpj-11-2015-0169.
- [22] Huet C. Application of variational concepts to size effects in elastic heterogeneous bodies. J Mech Phys Solid 1990;42:1995–2011.
- [23] Hill R. Elastic properties of reinforced solids some theoretical principles. J Mech Phys Solid 1963;11(5):357–72. https://doi.org/10.1016/0022-5096(63)90036-X (in English).
- [24] Jiang M, Jasiuk I, Ostoja-Starzewski M. Apparent elastic and elastoplastic behavior of periodic composites. Int J Solid Struct 2001;39(1):199–212. https://doi.org/10.1016/S0020-7683(01)00145-7.
- [25] Jiang M, Alzebdeh K, Jasiuk I, Ostoja-Starzewski M. Scale and boundary conditions effects in elastic properties of random composites. Acta Mech 2001;148(1-4):63-78. https://doi.org/ 10.1007/BF01183669.
- [26] Jiang M, Ostoja-Starzewski M, Jasiuk I. Scale-dependent bounds on effective elastoplastic response of random composites. J Mech Phys Solid 2001;49(3):655–73. https:// doi.org/10.1016/S0022-5096(00)00034-X.
- [27] Ostoja-Starzewski M, Kale S, Karimi P, Malyarenko A, Raghavan B, Ranganathan SI, et al. Scaling to RVE in random media. Adv Appl Mech 2016;49:111–211.
- [28] Sabet FA, Su FY, McKittrick J, Jasiuk I. Mechanical properties of model two-phase composites with continuous compared to discontinuous phases. Adv Eng Mater 2018;1800505.
- [29] Karpas LO, Ryan AM. Methods for additive manufacturing processes incorporating active deposition. 2014, US9102099B1.
- [30] D695-15, 2015. Standard test method for compressive properties of rigid plastics. West Conshohocken, PA: ASTM Standard: 2015.
- [31] Dizon JRC, Espera AH, Chen Q, Advincula RC. Mechanical characterization of 3D-printed polymers. Additive Manufacturing 2018;20:44–67. https://doi.org/10.1016/ j.addma.2017.12.002.
- [32] Wang L, Ju Y, Xie H, Ma G, Mao L, He K. The mechanical and photoelastic properties of 3D printable stress-visualized materials. Sci Rep 2017;7(1):10918. https://doi.org/10.1038/ s41598-017-11433-4.
- [33] Blaber J, Adair B, Antoniou A. Ncorr: open-source 2D digital image correlation matlab software. Exp Mech 2015;55(6):1105–22.
- [34] Yeoh OH. Some forms of the strain energy function for rubber. Rubber Chem Technol 1993;66(5):754–71.
- [35] Onck PR, Andrews EW, Gibson LJ. Size effects in ductile cellular solids. Part I: modeling. Int J Mech Sci Mar 2001;43(3):681–99. https://doi.org/10.1016/S0020-7403(00) 00042-4.
- [36] Andrews EW, Gioux G, Onck P, Gibson LJ. Size effects in ductile cellular solids. Part II: experimental results. Int J Mech Sci 2001;43(3):701–13. https://doi.org/10.1016/S0020-7403(00) 00043-6. 2001/12/01.
- [37] Abou-Ali AM, Al-Ketan O, Rowshan R, Al-Rub RA. Mechanical response of 3D printed bending-dominated ligament-based triply periodic cellular polymeric solids. J Mater Eng Perform 2019:1–11.
- [38] Abueidda DW, Bakir M, Abu Al-Rub RK, Bergström JS, Sobh NA, Jasiuk I. Mechanical properties of 3D printed polymeric cellular materials with triply periodic minimal

- surface architectures. Mater Des 2017;122:255–67. https://doi.org/10.1016/j.matdes.2017.03.018.
- [39] Alkhader M, Vural M. Mechanical response of cellular solids: role of cellular topology and microstructural irregularity. Int J Eng Sci 2008;46(10):1035–51. https://doi.org/10.1016/ j.ijengsci.2008.03.012. 2008/10/01.
- [40] Gross D, Seelig T. Micromechanics and homogenization. In: Fracture mechanics. Springer; 2018. p. 243–319.
- [41] Hashin Z, Shtrikman S. A variational approach to the theory of the elastic behaviour of multiphase materials. J Mech Phys Solid 1963;11(2):127–40. https://doi.org/10.1016/0022-5096(63) 90060-7.
- [42] Eggwertz S, Lind NC. Probabilistic methods in the mechanics of solids and structures: symposium stockholm, Sweden, 1984. Berlin, Germany: Springer Science & Business Media; 2012.
- [43] Brezny R, Green DJ. The effect of cell size on the mechanical behavior of cellular materials. Acta Metall Mater 1990;38(12):2517–26. https://doi.org/10.1016/0956-7151(90) 90263-G.
- [44] Puskas JE, Dos Santos LM, Fischer F, Götz C, El Fray M, Altstädt V, et al. Fatigue testing of implantable specimens: effect of sample size and branching on the dynamic fatigue properties of polyisobutylene-based biomaterials. Polymer 2009;50(2):591–7. https://doi.org/10.1016/ j.polymer.2008.10.061.
- [45] Bell D, Siegmund T. 3D-printed polymers exhibit a strength size effect. Additive Manufacturing 2018;21:658–65. https:// doi.org/10.1016/j.addma.2018.04.013.
- [46] Roach AM, White BC, Garland A, Jared BH, Carroll JD, Boyce BL. Size-dependent stochastic tensile properties in additively manufactured 316L stainless steel. Additive Manufacturing 2020;32:101090. https://doi.org/10.1016/ j.addma.2020.101090.
- [47] Farjam N, Nematollahi M, Andani MT, Mahtabi MJ, Elahinia M. Effects of size and geometry on the thermomechanical properties of additively manufactured NiTi shape memory alloy. Int J Adv Manuf Technol 2020;107(7–8):3145–54. https://doi.org/10.1007/s00170-020-05071 pt
- [48] Guessasma S, Belhabib S, Nouri H, Ben Hassana O. Anisotropic damage inferred to 3D printed polymers using fused deposition modelling and subject to severe compression. Eur Polym J 2016;85:324–40. https://doi.org/ 10.1016/j.eurpolymj.2016.10.030.
- [49] Blanco D, Fernandez P, Noriega A. Nonisotropic experimental characterization of the relaxation modulus for PolyJet manufactured parts. J Mater Res 2014;29(17):1876–82. https:// doi.org/10.1557/jmr.2014.200.
- [50] Choi K, Kuhn JL, Ciarelli MJ, Goldstein SA. The elastic moduli of human subchondral, trabecular, and cortical bone tissue and the size-dependency of cortical bone modulus. J Biomech 1990;23(11):1103–13.
- [51] Wheel MA, Frame JC, Riches PE. Is smaller always stiffer? On size effects in supposedly generalised continua. Int J Solid Struct 2015;67–68:84–92. https://doi.org/10.1016/ j.iisolstr.2015.03.026.
- [52] Polyjet materials data sheet, 2104. Stratasys; 2015.
- [53] Mueller J, Shea K, Daraio C. Mechanical properties of parts fabricated with inkjet 3D printing through efficient experimental design. Mater Des 2015;86:902–12.